Journal of Building Engineering 95 (2024) 110290

Contents lists available at ScienceDirect

Journal of Building Engineering

journal homepage: www.elsevier.com/locate/jobe

Enhancing the hydration and micromechanical properties of C_3A-gypsum systems with a plant-derived biomolecule

Yi Fang [a,b,c], Jialai Wang [c], Peiyuan Chen [d], Zhiang Chen [e], Liang Wang [d], Xin Qian [f], Shifu Liu [f,*], Jinxiang Hong [b]

[a] College of Civil and Transportation Engineering, Hohai University, Nanjing 210098, PR China
[b] State Key Laboratory of High Performance Civil Engineering Materials, Jiangsu Research Institute of Building Science Co., Ltd., Nanjing, 210008, Jiangsu, PR China
[c] Department of Civil, Construction, and Environmental Engineering, The University of Alabama, Tuscaloosa, AL, 35487, United States
[d] School of Civil Engineering and Architecture, Anhui University of Science and Technology, Huainan, 232001, Anhui, PR China
[e] Northeast Civil Aviation Professional Engineering Quality Supervision Station, Shenyang, 110043, Liaoning, PR China
[f] Key Laboratory of Infrastructure Durability and Operation Safety in Airfield of CAAC, Tongji University, Shanghai, 201804, PR China

ARTICLE INFO

Keywords:
Tannic acid
Tricalcium aluminate
Gypsum
Retardation
Hydration

ABSTRACT

This study investigates the influence of tannic acid (TA), a natural plant-based biomolecule, on the hydration of tricalcium aluminate (C_3A)-gypsum systems, aiming to elucidate its potential as a novel concrete strength enhancer. To this end, detailed investigations were conducted into the hydration and nano-mechanical properties of C_3A-gypsum system regarding the content of sulfate. In the absence of gypsum, the addition of TA accelerates the hydration of C_3A, leading to a 30.6 % increase in accumulated heat until 10 h. This acceleration is attributed to TA's intercalation with metastable hydration products, impeding their transformation into final hydrates (C_3AH_6). Characterization using XRD, TGA, and FTIR techniques confirms the presence of hexagonal hydrates as the main hydration products in C_3A-TA pastes, while the main hydration products in C_3A-DI pastes was cubic one. In scenarios involving gypsum, TA markedly retards the hydration of C_3A-gypsum mixtures, with SEM analysis indicating the promotion of AFt formation at low sulfate content while inhibiting its transformation to AFm. Furthermore, comprehensive nanoindentation results demonstrate that TA consistently enhances the micromechanical properties of C_3A-gypsum hydrates, irrespective of gypsum content. This study provides valuable insights into the mechanisms through which TA influences the hydration of C_3A-gypsum systems, offering promising avenues for enhancing the performance of concrete materials.

1. Introduction

Tricalcium aluminate (C_3A) is a crucial component of OPC, typically constituting 5–10 % of its mass. As the most reactive phase, C_3A significantly influences various properties of fresh cement mortar or concrete, including setting time, workability, and rheological characteristics [1,2]. In addition, C_3A positively affects the strength of hardened OPC cement matrix, increasing flexural strength and slightly decreasing compressive strength [3,4]. In situations where hardened cement paste or concrete is exposed to sulfate attack, the formation of calcium sulfoaluminate from C_3A can lead to expansion and potential damage to the paste [5]. Despite its potential

* Corresponding author.
E-mail address: sfliu@tongji.edu.cn (S. Liu).

https://doi.org/10.1016/j.jobe.2024.110290
Received 4 May 2024; Received in revised form 7 July 2024; Accepted 24 July 2024
Available online 26 July 2024

drawbacks, C_3A is indispensable in cement manufacturing, as it serves as a flux material, reducing the temperature required for clinker formation and aiding in the combination of lime with silica [7].

In the absence of sulfate, C_3A reacts with water to form hexagonal hydrates, namely C_2AH_8 and C_4AH_{13} [6,7]. However, these hexagonal hydrates are metastable and quickly convert to the stable cubic form, known as katoite (C_3AH_6), within an hour, resulting in rapid setting known as "flash set" [6–8]. To mitigate the issue of rapid setting in construction applications, gypsum is commonly added to clinker blends to inhibit C_3A dissolution and thereby slow down its hydration process [6,9,10]. In the presence of sulfate, the dissolution of C_3A is retarded primarily due to the formation of an aluminum-rich leached layer and subsequent adsorption of ion pair complexes [11,12]. Additionally, the precipitation of ettringite (AFt) on the surface of C_3A, as proposed by Joseph et al. [9], further impedes the reactivity of C_3A by blocking its active sites. Once the sulfate concentration drops below a critical threshold, AFt further reacts with C_3A to produce the stable hydration product monosulfate (AFm) [13,14]. This transformation from metastable hexagonal to stable cubic forms of calcium aluminate hydrate is accompanied by changes in crystal density and size. These alterations can result in diminished late-age strength of the cement paste due to the compromised adhesion and cohesion within the microstructure, as well as an increase in the porosity of the hardened cement paste.

The recent research has highlighted tannic acid (TA) as a potential concrete strength enhancer [15–18], inspired by the hierarchical structures found in protein-based materials in biological systems [19–21], which often exhibit superior strength and toughness. TA, a water-soluble natural polyphenol with high catechol content, has the ability to form complex molecular structures through multiple interactions such as hydrogen bonding, ionic bonding, and hydrophobic interactions [22–25]. This crosslinking ability allows TA to refine the pore structure of concrete, thereby enhancing its strength and durability [17,18]. Previous studies have also shown that polycarboxylate (PC) can intercalate aluminate hydrates during the hydration of C_3A, particularly in the absence of sulfate [26,27]. At low sulfate content, intercalation complexes with PC are formed in the hydrates, while at high sulfate concentrations, sulfate fills the interlayer space to produce modified-AFm [26]. In a similar vein, TA, with its phenolic carboxylate groups, may form intercalation complexes within the hydrates and may also directly intercalate with sulfate. This intercalation mechanism holds the potential to mitigate the loss of adhesion and cohesion within the microstructure during the transformation of calcium aluminate hydrates.

To advance our understanding, this study meticulously examined the influence of TA on the hydration of C_3A concerning gypsum content. Our objective was to deepen our comprehension of TA's potential as a novel enhancer for concrete strength. Specifically, we investigated the capability and mechanism of TA's integration into C_3A hydrates during the initial phases of cement hydration, recognizing the potential for such intercalation to augment the performance of C_3A hydrates. Detailed investigations were conducted into the hydration and nano-mechanical properties of C_3A-gypsum system using two distinct sulfate contents, including isothermal micro-calorimetry, X-ray Diffraction (XRD), Thermogravimetric analysis (TGA), Fourier Transform Infrared Spectroscopy (FTIR), and Scanning Electron Microscope (SEM) analysis. In addition, a grid of nanoindentation was deployed to assess the micromechanical properties of the C_3A-gypsum pastes. These investigations carry significant practical implications due to their profound impact on the early hydration and rheological behavior of OPC.

2. Experimental programs

2.1. Materials

Tricalcium aluminate (C_3A) of analytical purity was produced in laboratory following the poly(vinyl alcohol) (PVA) solution polymerization method described by Lee [28]. In this method, the precursors were analytically pure 0.2 mol/L $Ca(NO_3)_2{\cdot}4H_2O$ and 0.3 mol/L $Al(NO_3)_3{\cdot}9H_2O$ prepared using deionized water. Analytically pure PVA with a molecular weight of 80000 was mixed with deionized water to prepare a 5 wt% PVA solution using a 90 °C water bath. Subsequently, the resulting mixture underwent stirring in the water bath until complete removal of free water at 90 rpm. The obtained yellow porous material was subsequently subjected to

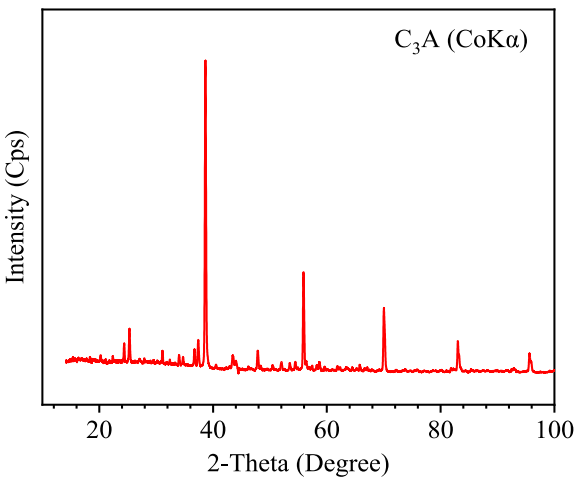

Fig. 1. XRD pattern of the synthesized anhydrous C_3A powder.

grinding and calcination at 1200 °C for 1 h with a heating rate of 3 °C/min. The resultant calcined white powder was further ground and subsequently sieved through a #200 sieve, which has a mean median particle size (d_{50}) of 25.84 μm as determined by a Beckman Coulter static light scattering (SLS) analyzer (Microtrac S3500). Fig. 1 shows the XRD pattern of the prepared C_3A, indicating a high purity over 98 %.

The gypsum ($CaSO_4{\cdot}2H_2O$, reagent grade) with a d_{50} of 5.85 μm and TA ($C_{76}H_{52}O_{46}$) with a purity of 98 % were procured from Alfa Aesar. A water/C_3A ratio of 3.0 was employed. The concentration of TA selected for this study was 0.5 wt% of C_3A for all systems. According to theoretical calculations, to form pure AFt, 1.91 g of gypsum per gram of C_3A is required, while for pure monosulfate formation, only 0.61 g of gypsum per gram of C_3A is needed [29]. In this study, two scenarios were examined regarding the amount of gypsum used in the mixtures, as shown in Table 1. The first scenario involved a lower amount of gypsum, with 0.5 g of gypsum per 1 g of C_3A, resulting in a SO_4^{2-}/C_3A molar ratio of 0.78. The second scenario involved a higher amount of gypsum, with 1.0 g of gypsum per 1 g of C_3A, resulting in a SO_4^{2-}/C_3A molar ratio of 1.57.

2.2. Characterization methods

2.2.1. Hydration heat

A TAM IV isothermal micro-calorimeter was used to measure the hydration kinetics of C_3A with setting at a constant temperature of 20 ± 0.1 °C. A water/C_3A ratio of 3 was adopted for this study. The deionized water or 0.5 % TA solution was mixed within the ampule for 1 min, following by sealed and then positioned into the testing chamber. Prior to initiating the recording, the system underwent an equilibration period of at least 15 min to ensure stability.

2.2.2. XRD

The samples were prepared with a water/C_3A ratio of 3 and cured under sealed conditions at room temperature. To halt the hydration process at specific ages, the samples underwent immersion in isopropanol for 24 h, followed by drying in a vacuum desiccator at room temperature for over 24 h. Subsequently, the dried samples were finely ground and sieved through a #200 sieve. Finally, these samples were placed in a desiccator with saturated $CaCl_2$ solution and a slight vacuum (~4 psi) at room temperature for further moisture control. The resulting powdered samples were then subjected to XRD, TGA, and FTIR analyses. XRD patterns were collected using a PANalytical X'Pert Pro MPD diffractometer equipped with a X'Celerator detector, operating in a 2θ configuration with CuKα radiation (λ = 1.54 Å). During data collection, a divergence slit size of 0.5° and a rotating sample stage were utilized. The scanned parameters of samples were in the 5–80° 2θ range, with an increment of 0.025° and at a speed of 2.5°/min.

2.2.3. TGA

TGA was employed to identify and quantify the hydration phases of C_3A-gypsum systems via a SDT600 thermogravimetric analyzer. For each test, the sample was first held at 30 °C for half hour, followed by heated from 40 °C to 1000 °C at 10 °C/min under a 100 mL/min nitrogen purge.

2.2.4. FTIR

The characteristic stretching vibrations of Al-O, S-O, and O-H bonds in C_3A hydrates can be detected by FTIR. The FTIR spectra were acquired utilizing a PerkinElmer Spectrum 2 spectrometer, which was outfitted with an attenuated total reflectance (ATR) accessory. The infrared spectra were captured across a wavenumber range spanning from 650 cm^{-1} to 4000 cm^{-1}.

2.2.5. SEM

The microstructure of the C_3A hydrates was analyzed using a Field Emission SEM (JSM-7000F) to capture secondary electron images. The SEM was operated at an accelerating voltage of 20 kV and a working distance (W.D.) of 10 mm.

2.2.6. Nanoindentation

A grid of nanoindentation was conducted to explore the impact of TA on the micromechanical properties of hydrated C_3A. The dosage of TA was 0.3 wt% of C_3A. The paste with a water/C_3A ratio of 2.0 and 0.3 wt% TA was prepared in cubic molds (20 mm × 20 mm × 20 mm) and cured at ambient temperature for 14 d. Subsequently, the paste was immersed and encapsulated using epoxy resin for the subsequent polishing by SiC sanding paper and diamond suspension on felt cloths [17]. A Hysitron TI950 nanoindenter equipped with a Berkovich diamond tip was employed to perform 400 indents in a 20 × 20 grid with a spacing of 10 μm. The measurement recipe, elastic modulus calculation, and the deconvolution process via Gauss Mixture Model (GMM) followed the methodology outlined in our previous study [16,17].

Table 1
Mix proportion of C_3A-gypsum pastes with and without TA.

Samples	C_3A (g)	Gypsum (g)	DI water (g)	TA (g)
C_3A-DI	1	–	3	–
C_3A-TA	1	–	3	0.005
G05C_3A-DI	1	0.5	3	–
G05C_3A-TA	1	0.5	3	0.005
G1C_3A-DI	1	1	3	–
G1C_3A-TA	1	1	3	0.005

3. Results and discussions

3.1. Hydration kinetic and hydration products of C3A-gypsum systems

3.1.1. Hydration in the absence of sulfate

When there is no sulfate, C_3A undergoes reaction with water, resulting in the formation of hexagonal plates of C_2AH_8 and C_4AH_{13} [6], as indicated by the following formulas (1) ~ (3). These hexagonal hydrates are metastable and undergo a conversion process to stable forms (C_3AH_6) within less than 1 h. The presence of the C_3AH_6 disrupts the protective barrier formed by the hexagonal hydrates, leading to a rapid progression of hydration once again [7].

$$C_3A + H \rightarrow C_4AH_{13} + C_2AH_8 (\text{Hexagonal hydrates}, 1260\ \text{J/g}) \quad (1)$$

$$C_4AH_{13} + C_2AH_8 \rightarrow 2C_3AH_6 (\text{Cubic hydrates}) \quad (2)$$

$$C_3A + H \rightarrow C_3AH_6\ (\text{Cubic hydrates}, 900\ \text{J/g}) \quad (3)$$

From Fig. 2, it is evident that TA does not exhibit a discernible retarding effect on the hydration of C_3A. In contrast, the higher heat release rate could be observed in C_3A-TA, indicating the enhancement in C_3A hydration by TA. This enhancement is further elucidated by the cumulative hydration heat depicted in Fig. 2b. Specifically, the C_3A-TA system demonstrates an accumulated hydration heat of 474 J/g until 10 h, which is 30.6 % higher than that in C_3A-DI. Considering the theoretically released heat of C_3A [7], it is noted that the reaction of cubic hydrates generates 40 % less heat compared to hexagonal hydrates. This suggests that the addition of TA might induce the stabilization of metastable C_3A hydrates and prevent the conversion of cubic one, verified by following XRD, TGA, and FTIR results.

To ascertain whether the metastable hydrates induced by TA ultimately transform into cubic hydrates, the C_3A hydrates in the presence of TA at 3 d and 11 d were analyzed by XRD, as depicted in Fig. 3 and Table 2. The addition of TA notably decreases the hydrogarnet (C_3AH_6) content while increasing the presence of C_2AH_8 and C_4AH_{13} at 3 d. This observation stems from TA's inhibition of the transition products' conversion into C_3AH_6. Metastable hydration products such as C_2AH_8 and C_4AH_{13} can be stabilized by TA, as evidenced. In such cases, the transformation of hexagonal hydrates is hindered due to TA molecules' adsorption on the grain surface. Intercalation of TA in aluminate hydrates (e.g., C_2AH_8 and C_4AH_{13}) might occur during C_3A hydration [26], a process known to stabilize hexagonal hydrates over cubic hydrates, as observed with other organic compounds [30]. Further elucidation of the precise mechanism will be pursued in subsequent investigations. Additionally, TA's presence leads to a significant reduction in the percentage of C_3AH_6 and a noticeable decrease in the crystallization degree of C_4AH_{13}, as evidenced by peak broadening. Moreover, the crystallization degree of C_4AH_{13} is lower than that of C_3AH_6, resulting in broader and less sharp peaks in the XRD patterns.

In order to quantitatively assess the differences in hydration products of C_3A, TGA analysis was utilized and the results are depicted in Fig. 4. The weight loss of the main peaks was calculated based on the following formulas:

$$W_{[H_2O]} = \frac{M_{40} - M_{1000}}{M_{40}} \times 100(\%) \quad (4)$$

$$W_{[C_2AH_8/C_4AH_{13}]} = \frac{(M_{60} - M_{175})_{tangential}}{M_{40}} \times 100(\%) \quad (5)$$

$$W_{[C_3AH_6]} = \frac{(M_{175} - M_{370})_{tangential}}{M_{40}} \times 100(\%) \quad (6)$$

where M_{40}, M_{60}, M_{175}, M_{370}, and M_{1000} are the measured mass at the temperature of 40 °C, 60 °C, 175 °C, 370 °C, and 1000 °C, respectively.

The total mass losses of the C_3A-DI and C_3A-TA at 3 d are 28.5 % and 35.6 %, respectively, while the weight loss of C_3A-TA at 11 d is 34.9 %. Since the mass loss of C_3A hydrate was mainly came from the evaporation of bounding water, the total mass loss could partly

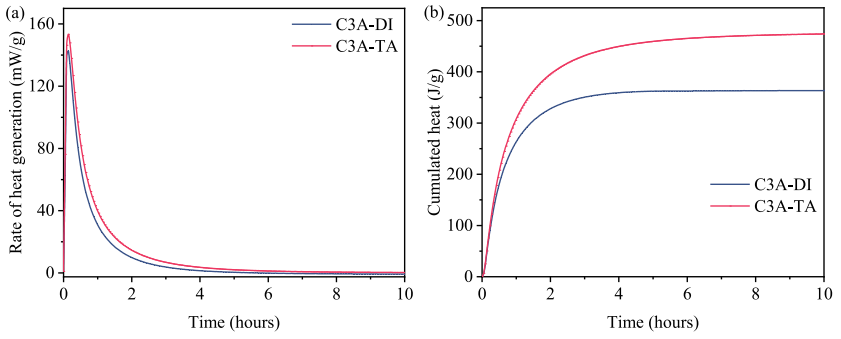

Fig. 2. Effect of TA on the hydration kinetics of pure C_3A pastes: (a) rate of heat generation; (b) cumulated heat.

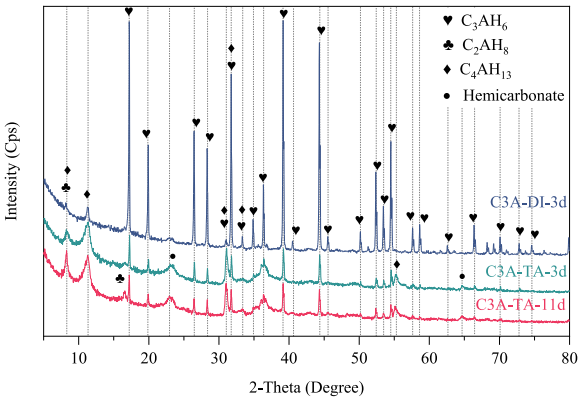

Fig. 3. Effect of TA on the mineral compositions of pure C_3A hydrates at 3 d and 11 d (hemicarbonate: $Ca_4Al_2O_6(CO_3)_{0.5}(OH)\cdot 11.5H_20$).

Table 2
Main hydration products of C_3A hydrates in presence of TA.

System	Main Products		
C_3A-DI-3d	C_2AH_8 (little)	C_4AH_{13} (much less)	C_3AH_6 (most)
C_3A-TA-3d	C_2AH_8	C_4AH_{13}	C_3AH_6
C_3A-TA-11 d	C_2AH_8 (increased)	C_4AH_{13}	C_3AH_6

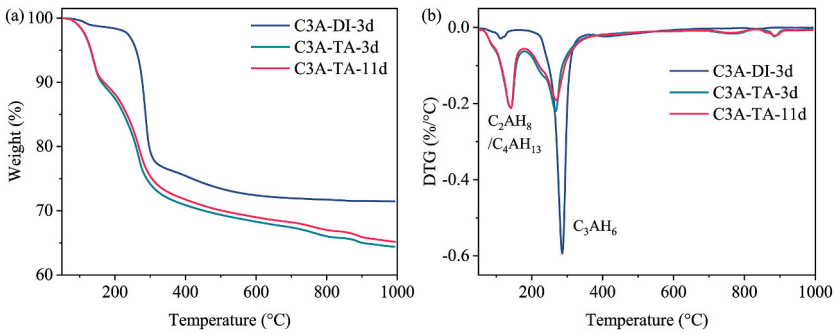

Fig. 4. Effect of TA on the TGA results of pure C_3A hydrates at 3 d and 11 d: (a) TGA; (b) DTG.

indicate the composition of the hydration products. The theoretical water loss of C_2AH_8, C_4AH_{13}, and C_3AH_6 can be calculated based on the molar mass, and the results are 40.2 %, 41.8 %, and 28.6 %, respectively. Thus, the addition of TA leads to more metastable products in C_3A hydrates.

The amount of each phase in C_3A hydrates can be calculated based on the water loss occurred in peaks shown in DTG curves, as detailed in Table 3. The addition of TA significantly alters the composition of the C_3A hydrates at 3 d. Detailly, the mass loss caused by C_3AH_6 was reduced from 20.0 % to 9.3 %, while the mass loss caused by metastable hydration products were increased from 0.8 % to 6.8 %. These results align well with the XRD analysis. Furthermore, it was found that there is little phase conversion occurred from 3 d to 11 d in C_3A-TA, as revealed by Table 3. This indicates the intercalation of TA has a lasting effect on the phase transformation of C_3A hydration.

3.1.2. Hydration in the presence of sulfate

Fig. 5 demonstrates the influence of TA on the hydration evolution of C_3A-gypsum systems, emphasizing the critical role of sulfate

Table 3
The weight loss of main peaks shown in DTG curves of C_3A-DI and C_3A-TA.

T (°C)	Sources of weight loss peaks	Weight loss (%)		
		C_3A-DI (3 d)	C_3A-TA (3 d)	C_3A-TA (11 d)
60–175	Decomposition of C_2AH_8 and C_4AH_{13}	0.8	6.8	6.7
175–370	Decomposition of C_3AH_6	20.0	9.3	9.5

in mitigating flash setting. In scenarios with low sulfate content (SO_4^{2-}/C_3A molar ratio of 0.78), the initial rapid hydrolysis of C_3A and subsequent AFt precipitation are succeeded by a 3-h period of slower reaction [6,29], followed by AFm nucleation and growth, as evidenced by a significant peak in the heat evolution curve (Fig. 5a). Upon the addition of TA, the duration of the slow reaction period extends from 3 h to 48 h. Furthermore, the primary peak associated with AFm formation is attenuated, with its intensity decreasing from 86 mW/g to 32 mW/g. This suggests that TA impedes the transformation from AFt to AFm under low sulfate conditions. Notably, the accumulated heat until 72 h increases to 798 J/g, comparable to the 812 J/g observed in groups without TA. Such retardation may arise from the adsorption of chelate complexes of TA and Ca^{2+} on the grain surface [16–18], resulting in a denser coating compared to samples without TA.

In the scenario where the sulfate content is high (SO_4^{2-}/C_3A molar ratio of 1.57), the onset of the second peak in G1C_3A-DI is delayed until 10 h. The accumulated heat in G1C_3A-DI until 72 h rises to 927 J/g. However, there is no indication of a second peak appearing in G1C_3A-TA. This implies that TA has impeded the reaction between AFt and C_3A. Consequently, the accumulated heat until 72 h in G1C_3A-TA is only 323 J/g. As shown in Fig. 5c, even when the hydration time is extended to 168 h, the accumulated heat only increases steadily to 405 J/g without exhibiting another peak. It suggests that TA molecule exerts a significant retardation effect on the hydration process of C_3A-gypsum systems, potentially making them suitable candidates as green retarders for calcium sulfoaluminate cements.

As shown in Fig. 5, the hydration process of C_3A at low sulfate concentration appears to reach near-completion after 3 d, regardless of the addition of TA. Consequently, samples collected at 3 d were selected for XRD analysis to examine their final hydrates. Additionally, to identify intermediate hydrates following the initial heat-releasing peak observed in G05C_3A-TA, samples at 1 day were also subjected to XRD analysis.

As illustrated in Fig. 6, the incorporation of TA does not alter the composition of hydration products at 3 d. The hydration products of C_3A are primary monosulfate and hemi-carbonate ($C_4Ac_{0.5}H_{12}$) with the presence of low sulfate concentration. All the gypsum has been consumed by C_3A for generating AFt, while the residual C_3A reacts with a portion of the AFt to generate monosulfate. The presence of Hc arises from the partial substitution of interlayer OH^- or SO_4^{2-} by CO_3^{2-} [31], likely due to the contamination from atmospheric CO_2 during the sample preparation [6]. The formation of monosulfate is suppressed in the presence of $CaCO_3$ [32]. Instead, the rapid formation of Hc occurs. Analysis of the sample from G05C_3A-TA at 1 d reveals the presence of unhydrated C_3A, unreacted gypsum, and a minor amount of monosulfate and Hc. This suggests that the initial peak represents the dissolution peak and AFt formation, while the subsequent peak is a combination of peaks corresponding to monosulfate and Hc formation, as indicated in Fig. 5a. Although TA significantly delays the hydration rates, it is presumed to have minimal impact on the fundamental mechanism of C_3A hydration. Further studies will be conducted to elucidate the detailed reaction mechanism.

Since the hydration of C_3A at high sulfate concentration (SO_4^{2-}/C_3A molar ratio of 1.57) with TA remains incomplete after 7 d, samples collected at this time point were employed for XRD analysis. As depicted in Fig. 6, the hydrates of G1C_3A primarily consist of AFt and Hc ($C_4Ac_{0.5}H_{12}$). In contrast, the addition of TA results in a substantial amount of unreacted C_3A and gypsum in the pastes. Most of the hydrates comprise AFt, with only a minimal amount of Hc formed. This indicates that the formation of AFt following the

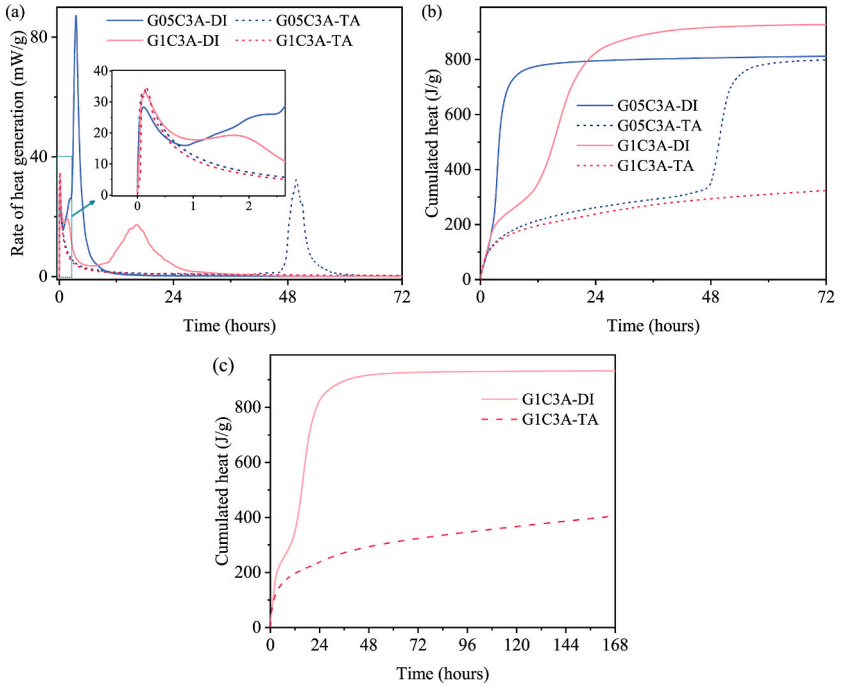

Fig. 5. Heat evolution of hydration in C_3A-gypsum system: (a) Rate of heat generation until 72 h; (b) Cumulated heat until 72 h; and (c) Cumulated heat until 168 h.

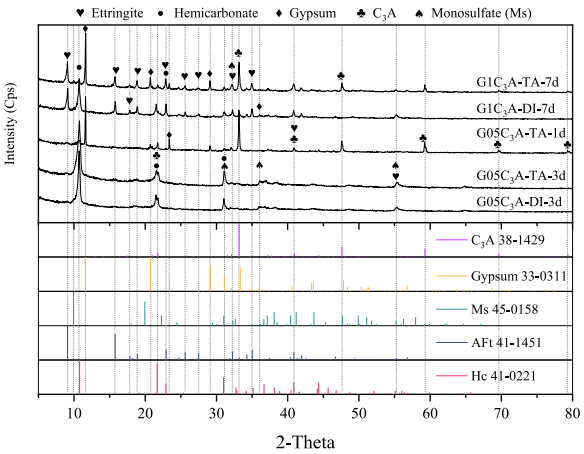

Fig. 6. Effect of TA on the mineral composition of the C_3A-gypsum hydrates at different ages (Hc: hemicarbonate, $Ca_4Al_2O_6(CO_3)_{0.5}(OH)\cdot 11.5H_2O$).

initial dissolution peak is relatively slow, consistent with the low but sustained heat release rate observed over an extended period in Fig. 6a. The presence of gypsum in G1C_3A-TA suggests that the addition of TA significantly retards the hydration of C_3A. The formation of AFt is not yet complete, leaving room for potential Hc-AFm formation subsequent to AFt production. Moreover, to precisely quantify the amount of hydration products, TGA analysis was conducted on these hydrates.

Fig. 7 illustrates the TGA results of the hydration products of C_3A-gypsum. The water loss associated with gypsum ($CaSO_4$ $2H_2O$) occurs within the temperature range of approximately 100 °C–140 °C, followed by a transformation to hemihydrate ($CaSO_4$ $0.5H_2O$) within the temperature range of 140 °C–150 °C, and finally to anhydrite ($CaSO_4$) at higher temperatures. AFt ($3CaO\ Al_2O_3\ 3CaSO_4\ 32H_2O$) shows a loss of the water between the columns at around 100 °C (~36 wt%), while the dehydration through dihydroxylation occurs between 200 °C and 400 °C, with the primary weight loss observed at approximately 240 °C (~9 wt%) [33]. Monosulfate (Ms) showed the dehydration steps of the six interlayers between 60 and 200 °C, while the water loss from the octahedral layer occurs from 250 to 350 °C [33,34]. Regarding hemicarbonate [$4CaO\ Al_2O_3\ (CO_3)_{0.5}\ 12H_2O$, or $Ca_4Al_2O_6(CO_3)_{0.5}(OH)\cdot 11.5H_2O$], the removal of five interlayer H_2O molecules is evident between 60 °C and 200 °C [31], with the primary weight loss occurring near 150 °C, followed by the elimination of H_2O molecules from the octahedral layer at around 840 °C. The theoretical water loss of gypsum, AFt, Ms, and Hc can be calculated based on the molar mass, and the results are 20.9 %, 45.9 %, 34.7, and 38.3 %, respectively. Given the substantial

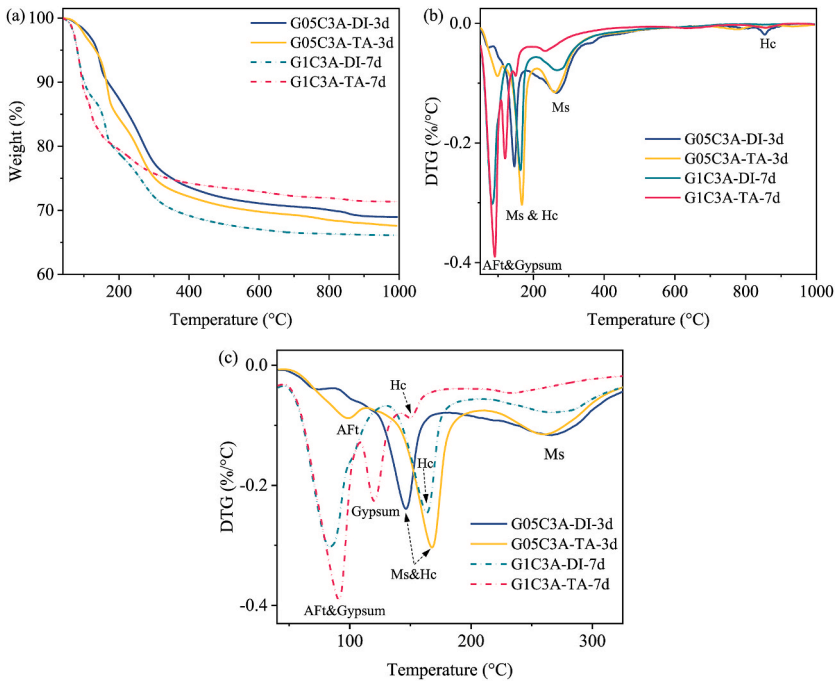

Fig. 7. Effect of TA on the TG analysis of the C_3A-gypsum mixtures at different ages: (a) TGA; (b) DTG; (c) Enlarged DTG curves.

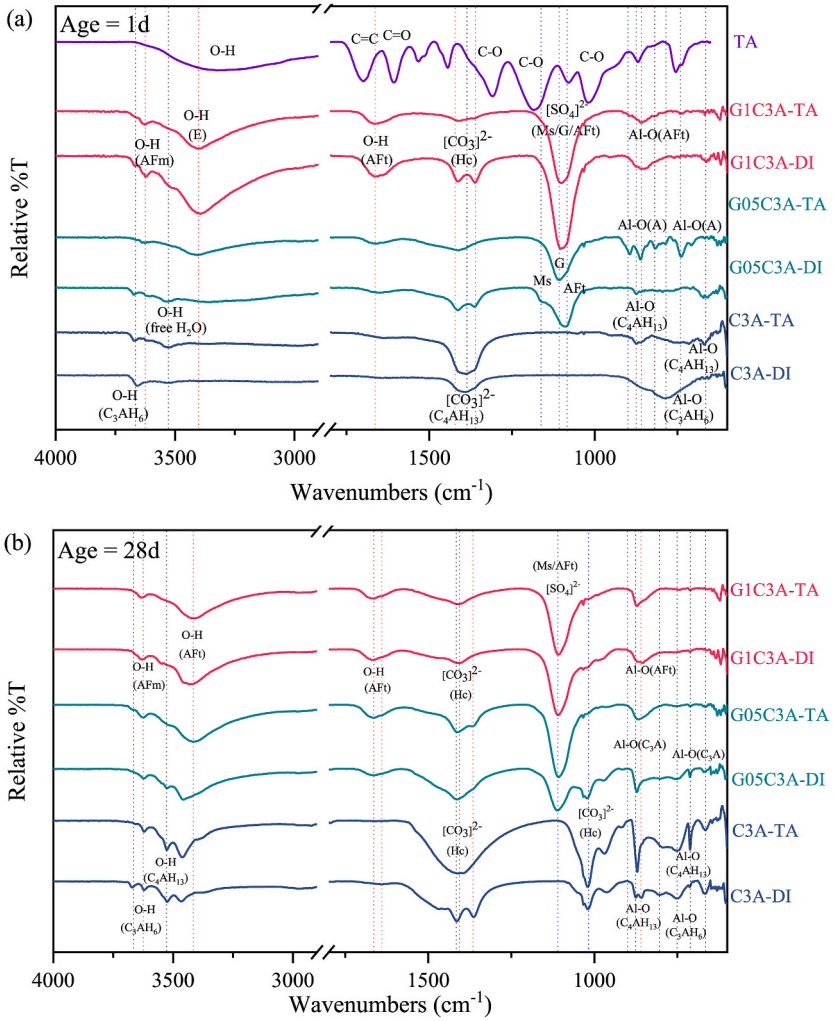

Fig. 8. Effect of TA on the FTIR patterns of C_3A-gypsum mixtures at different curing ages: (a) 1 d; (b) 28 d.

overlap in the decomposition temperatures of these three compounds, it is challenging to accurately determine the content of each compound solely from the TGA results presented here.

As shown in Fig. 7a, it can be found that the addition of TA generates more hydration product of C_3A in presence of low sulfate content, as evidenced by the increased total weight loss at 3 d from 21.0 % to 22.4 %. This might because TA facilitates the formation of monosulfate and Hc ($C_4Ac_{0.5}H_{12}$), as indicated by the higher peak around 31.1° shown in XRD analysis (Fig. 6). Besides, the decomposition peak temperature for monosulfate and Hc in G05C_3A is increased from 158 °C to 170 °C by TA. This suggests that TA enhances the thermal stability of monosulfate and Hc, which might be attributed to TA's hydrogen and ionic bonding with the hydration products. Furthermore, comparing with G05C_3A-DI, the group G05C_3A-TA contains more AFt phase, which will be verified by the SEM results shown in Fig. 9.

In cases of high sulfate content, the main hydrates of G1C3A-DI at 7 d were AFt and hemicarbonate, which is consistent with XRD result. The addition of TA decreases the amount of hydration products, as evidenced by the decreased total weight loss at 7 d from 33.9 % to 28.6 %. Besides, G1C_3A-TA contains much less hemicarbonate found in DTG peaks between 150 °C and 200 °C. This can be attributed to the significant retardation of TA on the hydration of C_3A-gypsum system shown in hydration evolution curves (Fig. 5). As a result, a notable presence of gypsum is observed in G1C_3A-TA. The coexistence of gypsum in G1C3A-TA suggests that the formation of AFt is incomplete.

3.2. FTIR

Fig. 8 presents the FTIR results of C_3A-gypsum pastes at 1 d and 28 d. The spectral peaks can be assigned based on the characteristic vibrational modes associated with specific chemical groups, including SO_4^{2-}, CO_3^{2-}, O-H, and Al-O groups, as detailed in Table 4. The S-O stretching vibration of SO_4^{2-} appears in the range of 1150–1100 cm^{-1}, with distinct peaks observed at 1150 cm^{-1} for monosulfate, 1115 cm^{-1} for AFt, and 1117 cm^{-1} for gypsum [35–37]. The presence of $C_4Ac_{0.5}H_{12}$ is primarily identified by the asymmetric

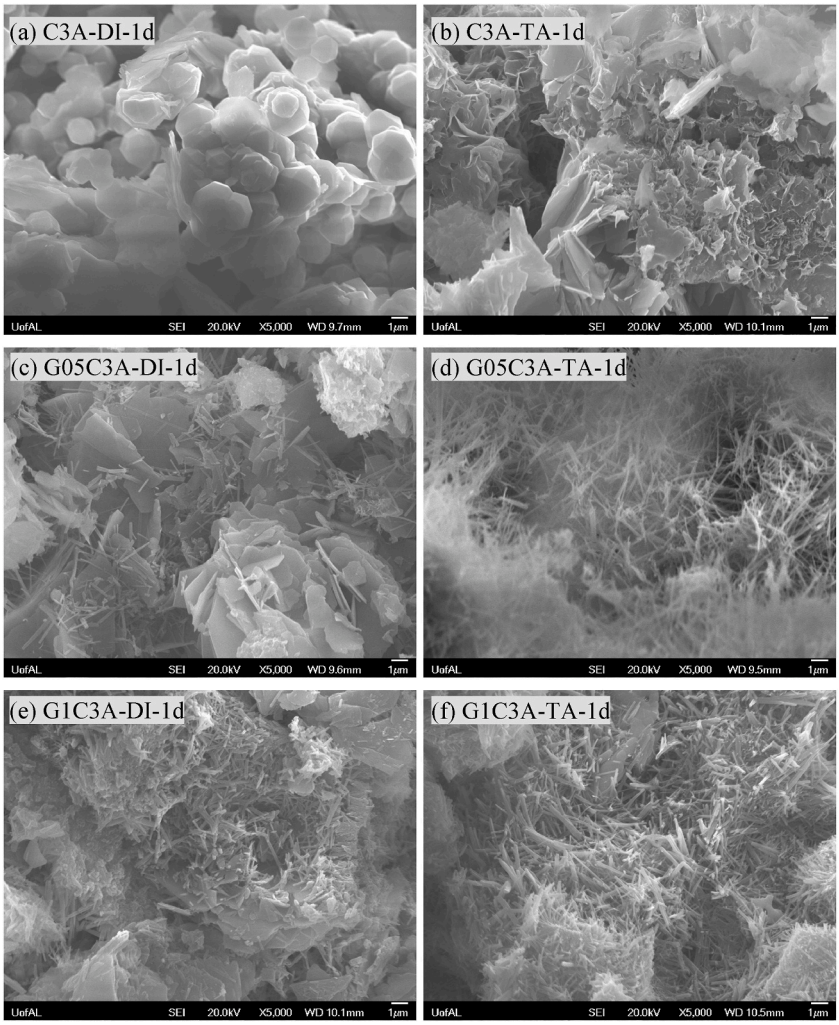

Fig. 9. Effect of TA on the SEM images of hydrated C_3A-gypsum pastes at 1 d.

Table 4
Main peak assignment for the FTIR spectra of C_3A-gypsum hydrates with or without TA (wavenumber: cm^{-1}).

Assignment		O-H		CO_3^{2-}			SO_4^{2-}	Al-O	
C_3A-DI	1 d	3659	–	1391	–	–	–	786	–
	28 d	3525/3466		1414	1363	1019	–	875/858	751/666
C_3A-TA	1 d	3529	–	1391	–	–	–	–	667
	28 d	3526/3462	–	1412	–	1020	–	871	751/712/666
G05C_3A-DI	1 d	3373	1653	1414	1364		1088	–	672
	28 d	3525/3457	–	1412	–	1022	1111	872	712/671
G05C_3A-TA	1 d	3406	1661	1413	–	–	1109	862	739
	28 d	3415	1664	1412	1368	–	1107	871	–
G1C_3A-DI	1 d	3393	1662	1415	1362	–	1102	859	662
	28 d	3422	1665	1408	–	–	1109	855	–
G1C_3A-TA	1 d	3405	1663	1414	–	–	1102	860	–
	28 d	3407	1664	1407	–	–	1108	871	–

stretching of CO_3^{2} at 1365 cm^{-1} and 874 cm^{-1} [37]. The band near 3600 cm^{-1} is assigned to the vibration of OH in calcium aluminum hydrate (C_4AH_{19}), carbonated species (Hc), or other AFm hydrates [38]. In addition, O-H bands manifest in the region of 1600–1700 cm^{-1} and above 3000 cm^{-1} [37]. Aluminate bands arising from Al-O bending are positioned near 855 cm^{-1} in AFt and 786 cm^{-1} in C_3AH_6. The Al-O bending in AlO_4-tetrahedral groups is observed near 600-900 cm^{-1} [37].

As shown in Fig. 8a, the hydration products of C_3A-DI at 1 d primarily consist of C_3AH_6, as indicated by the broader peak near 786 cm^{-1} observed in the spectra. However, the addition of TA significantly alters the mineral compositions of C_3A hydrates, evident from

the broader peak near 1391 cm^{-1} resulting from the carbonation of C_4AH_{13} and the shallow peak near 667 cm^{-1}. As the curing age progresses to 28 d, it is observed that the CO_3^{2-} group in C_3A-TA shifts from 1391 cm^{-1} to 1412 cm^{-1}, accompanied by a deeper and broader peak in the spectra. This difference will be further elucidated through the SEM images presented in the subsequent section.

In cases of low sulfate content, as depicted in Fig. 8a, the hydration products predominantly include monosulfate, AFt, and small amounts of C_3AH_6, C_4AH_{13}, and $C_4Ac_{0.5}H_{12}$. TA leads to an abundance of unhydrated C_3A and gypsum peaks in the hydration products, as observed in G05C3A-TA at 1 d. This significant retardation effect of TA on the hydration of C_3A-gypsum has been explained in previous sections. Comparing with G05C_3A-DI, the group G05C_3A-TA at 1 d exhibits a weakened peak near 1413 cm^{-1}, indicating reduced formation of AFt and AFm. However, as the curing age progresses to 28 d, the retardation effect of TA appears to diminish, as evidenced by the stronger peak near 1107 cm^{-1} assigned to AFt or AFm. Additionally, there is less Hc observed in G05C_3A-TA, suggesting that TA might resist the carbonation of the final hydration products of C_3A at low sulfate content.

In cases of high sulfate content, the spectra of G1C_3A-DI and G1C_3A-TA at 1 d was similar except the significant difference around 1415 cm^{-1} and 1362 cm^{-1}. This similarity arises because the additional sulfate further slows down the hydration of C_3A. Consequently, gypsum becomes abundant in the hydration products, with AFt being the main hydration product and AFm being negligible after 1 d. The presence of a significant peak of O-H near 3625 cm^{-1} indicates the retardation effect of gypsum. Moreover, the presence of TA causes a weakened peaks of AFt near 1662 cm^{-1}, indicating the retardation of TA. However, these differences were diminished at 28 d, which means TA just delays the hydration of G1C_3A. The observed difference in hydration products between scenarios with G1C_3A and G05C_3A at 28 d warrants further investigation. Future research will delve into this phenomenon to better understand its underlying mechanisms and implications.

3.3. Microstructure

Fig. 9 presents the SEM images of pure C_3A hydrates at 1 d. The diverse morphologies of different hydration products of C_3A enable

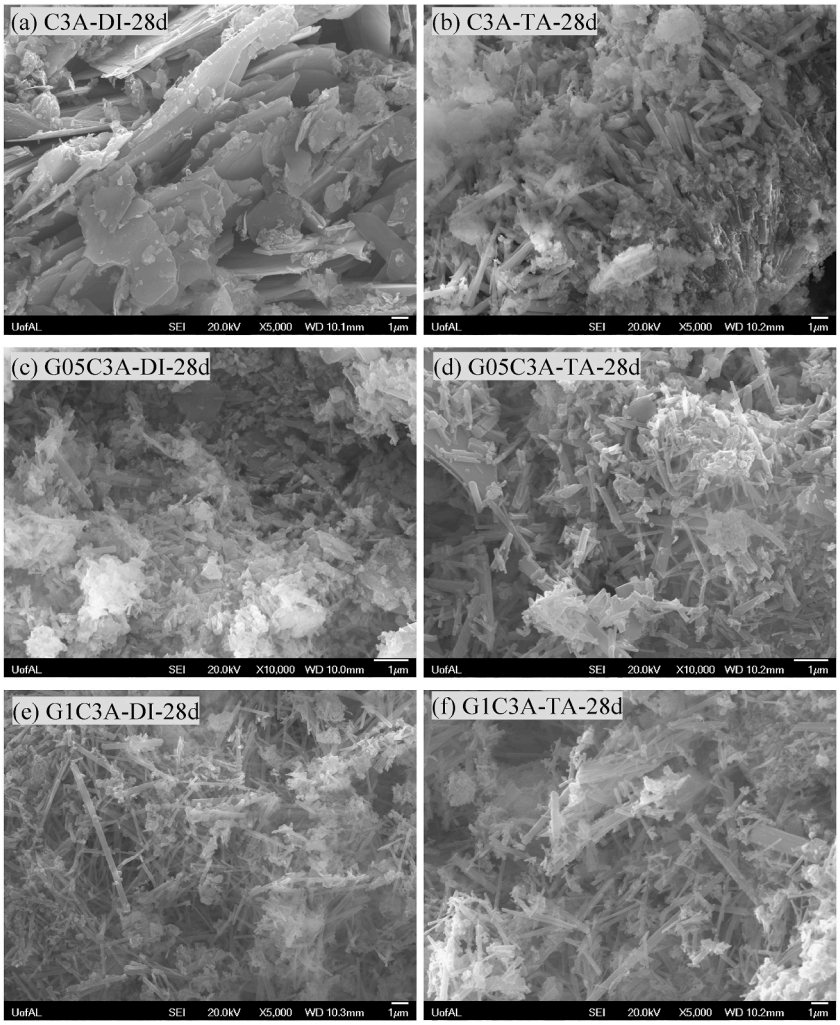

Fig. 10. Effect of TA on the SEM images of hydrated C_3A-gypsum pastes at 28 d.

their separation easily. The morphology of C_3AH_6 is cubic crystals, while C_4AH_{13} or C_2AH_8 are hexagonal crystals. As shown in Fig. 9a, the predominant hydrates in C_3A-DI are C_3AH_6 with a small amount of C_4AH_{13}. Upon the involvement of TA in the hydration process, the predominate hydrates in C_3A-TA is C_4AH_{13}, as illustrated in Fig. 9b. This is because TA can stabilize these hexagonal hydrates and prevent the transformation to C_3AH_6, as discussed in the previous sections. Interestingly, even the curing age progresses to 28 d, the main hydration product of C_3A-TA is still hexagonal hydrates, rather than cubic hydrates.

In cases of low sulfate content (G05C_3A), the main hydration product is AFm and a small amount of AFt, in which the morphology of AFm and AFt is hexagonal plate and needle shape, as observed in Fig. 9c. In the presence of TA, the morphology of C_3A-gypsum hydrates was significantly changed, as shown in Fig. 9d, where the main hydrates in G05C_3A-TA are needle-shape. This is because the retardation effect induced by TA delays the formation of AFt, leaving abundant unreacted gypsum, as indicated by XRD results. In cases of high sulfate content (G1C_3A), the primary hydration product of C_3A becomes needle-shaped and could be assigned to AFt, as shown in Fig. 9e. A small amount of hexagonal AFm is also present due to sulfate depletion during hydration. Conversely, in the presence of

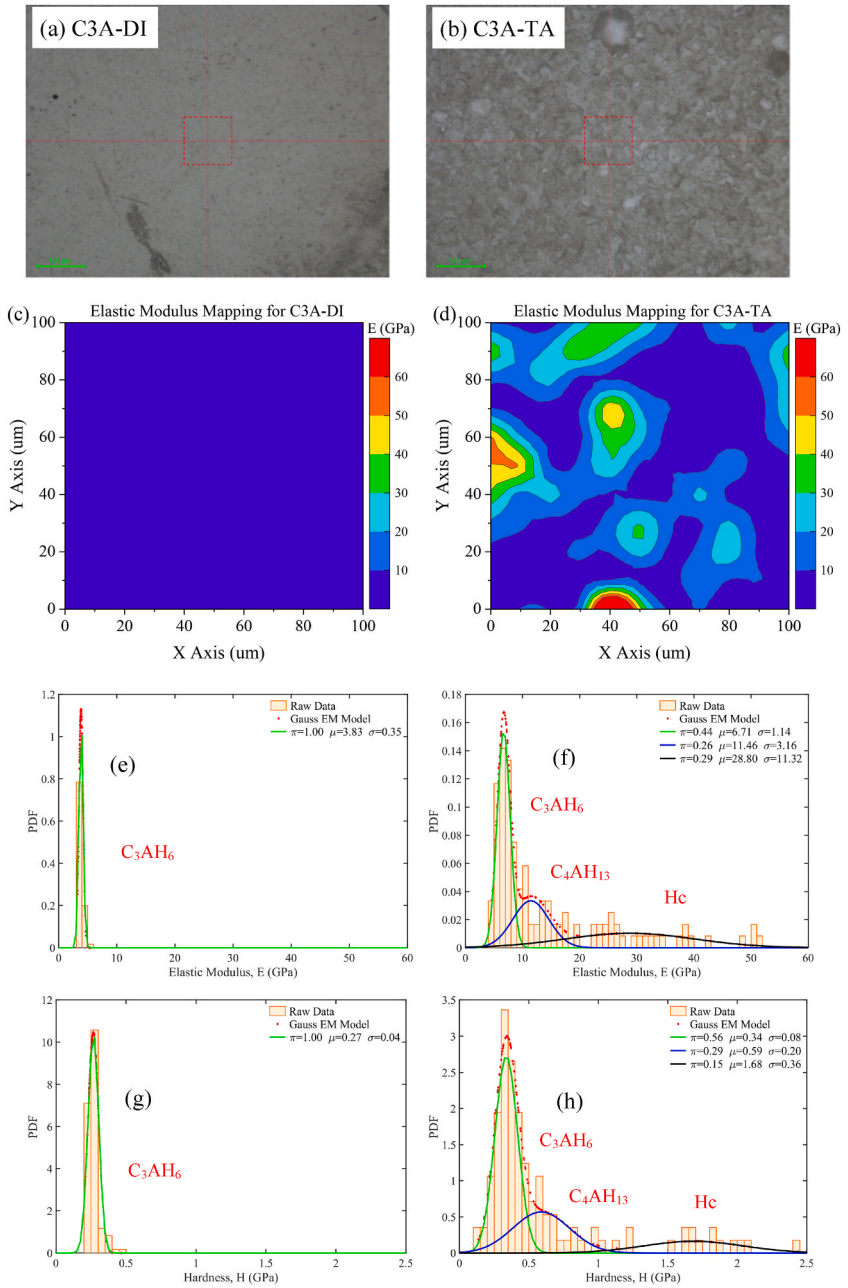

Fig. 11. The nanoindentation results of C_3A-DI and C_3A-TA pastes: (a)&(b) microscope images; (c)&(d) the contour mapping of elastic modulus; (e)&(f) the deconvolution results of *Es*; (e)&(f) the deconvolution results of hardness.

TA, the hydration product in G1C_3A-TA consists solely of AFt.

The SEM investigation was extended to examine the morphologies of the hydrates after curing for 28 days, aiming to discern any differences in the final hydrates, as depicted in Fig. 10. In the absence of gypsum, the hydration products of C_3A manifest as plate-like carbonates, as illustrated in Fig. 10a. Conversely, in the presence of TA, the morphology of the hydration products shifts to prism-like carbonates (Fig. 10b), leading to the enhancement of micromechanical properties as discussed in later section. With the inclusion of gypsum, the morphology of the final hydrates appears similar, characterized by needle-shaped structures, as shown in Fig. 10(c ~ f). This similarity suggests that the presence of gypsum plays a dominant role in determining the morphology of the final hydrates, despite the potential retarding effects induced by TA.

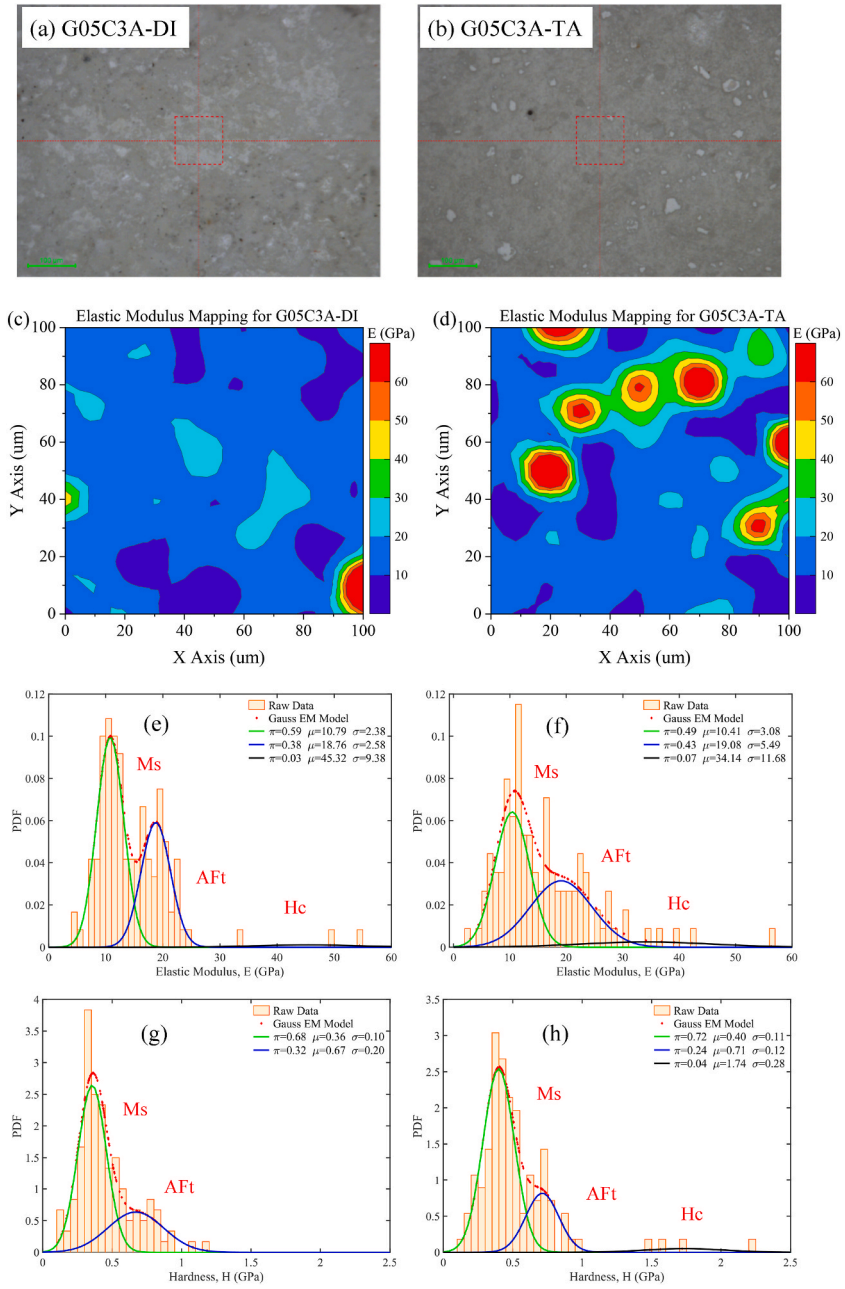

Fig. 12. The nanoindentation results of G05C_3A-DI and G05C_3A-TA pastes: (a)&(b) microscope images; (c)&(d) the contour mapping of elastic modulus; (e)&(f) the deconvolution results of *Es*; (e)&(f) the deconvolution results of hardness.

3.4. Nanoindentation

3.4.1. In the absence of sulfate

As shown in Fig. 11, the nanoindentation results of pure C_3A hydrates revealed significant differences induced by the addition of TA compared to C_3A-DI. Optical images show a granular texture on the surface of C_3A-TA, contrasting with the flat texture observed in C_3A-DI. This difference is likely attributable to distinct hydration products, C_3AH_6 (cubic) and C_4AH_{13} (hexagonal). While C_3AH_6 crystals tend to form a flat surface, the arrangement of C_4AH_{13} plates is more random. Consequently, there is a notable contrast in the elastic modulus mapping. In C_3A-DI, the distribution of elastic modulus remains below 5 GPa for all indent areas, whereas C_3A-TA hydrates exhibit a wider distribution ranging from 0 to 60 GPa.

The GMM deconvolution analysis revealed three distinct phases of pure C_3A hydrates: C_3AH_6, C_4AH_{13}, and Hc, characterized by varying elastic moduli, with C_3AH_6 having the lowest and Hc the highest. In the deconvolution results, π, μ, and σ denote the volume fraction, mean value, and standard deviation of each phase, respectively. Although the theoretical elastic modulus of C_3AH_6 calculated by molecular dynamics (MD) simulations is 93.8 GPa [39,40], the elastic modulus of C_3AH_6 cement pastes measured using a Vickers indenter was only 0.9 GPa [41]. This discrepancy arises because the elastic modulus measured by nanoindentation represents an average value of both the hydrates and capillary pores. The packing density of the hydrates significantly influences these values. The theoretical elastic modulus of AFm is approximately 30 GPa, as determined by thermodynamic and MD simulations [42]. Since the phase C_4AH_{13} is also referred to as OH-AFm, its elastic modulus should be around 30 GPa. Additionally, the elastic modulus of Hc has been calculated to be 34.5 GPa via thermodynamic simulation [42].

As depicted in Fig. 11e, the dominant peak in C_3A-DI corresponds to the cubic C_3AH_6 hydrates, indicating the transformation from hexagonal to cubic hydrates, which typically leads to increased porosity and disruption of the microstructure, resulting in a lower average elastic modulus of 3.83 GPa. Conversely, in C_3A-TA, the failure of this conversion leads to a denser microstructure with lower porosity (Fig. 11f), significantly enhancing the average elastic modulus to 14.28 GPa. Additionally, the presence of another peak assigned to Hc [$C_4Ac_{0.5}H_{12}$] in the deconvolution results of C_3A-TA was supported by previous analyses. The existence of Hc further contributes to the elevated elastic modulus of C_3A-TA pastes. However, despite the presence of some Hc in C_3A-DI, as indicated by XRD, TGA, and FTIR analyses, the poor microstructure still results in a relatively low elastic modulus in C_3A-DI.

As shown in Fig. 11g and h, the deconvolution results of hardness show the similar trend as that of elastic modulus. As a result, the average hardness of C_3A paste was improved from 0.27 GPa to 0.61 GPa via the incorporation of TA molecule.

3.4.2. In the presence of sulfate

Fig. 12 presents the effect of TA on the nanoindentation results of C_3A pastes with low sulfate content. As shown in Fig. 12a and b, the optical images of G05C_3A-DI and G05C_3A-TA show slight difference on the color. However, there is a notable disparity in the distribution of elastic modulus, particularly in areas with high stiffness ($E > 60$ GPa) attributed to the unhydrated C_3A or gypsum, indicating the retarded hydration of C_3A-gymsum system via TA.

The GMM deconvolution analysis revealed three distinct phases of C_3A-gypsum hydrates: monosulfate [43], AFt [44], and Hc [30], characterized by varying elastic moduli, with monosulfate having the lowest and Hc the highest. The typical elastic modulus of AFt is around 20 GPa from nanoindentation analysis [44,45]. Although the theoretical elastic modulus of monosulfate is approximately 30 GPa [42,46], the conversion of AFt to monosulfate leads to increased porosity and disruption of the microstructure, resulting in a quite low value. According the Zhao's thermodynamic simulation results [42], the elastic modulus of Hc has been calculated to be 34.5 GPa, while that of AFt is 28.3 GPa. In addition, the formation of Hc is much easier than that of monosulfate in the presence of $CaCO_3$ due to the stability [32].

As shown in Fig. 12e and f, the incorporation of TA leads to an augmentation in the quantity of AFt and Hc phases, accompanied by a reduction in monosulfate. Specifically, the volume fraction of monosulfate decreased from 0.59 to 0.49, whereas the volume fraction of AFt increased from 0.38 to 0.43. Furthermore, the average elastic modulus for the hydrates, falling within the range of $E \leq 60$ GPa, exhibited an increase from 14.85 GPa to 15.70 GPa. This enhancement can be attributed to the organic carboxylate groups in TA, which have the potential to facilitate the formation of Hc and AFt. Consequently, this process may help alleviate the disruption of the microstructure, leading to a denser microstructure and thereby contributing to the observed increase in the average elastic modulus.

As shown in Fig. 12g and h, the deconvolution results of hardness show the different trend as that of elastic modulus. Specifically, the volume fraction of monosulfate increased from 0.68 to 0.72, whereas the volume fraction of AFt decreased from 0.32 to 0.24. However, the average hardness of G05C_3A paste was improved from 0.46 GPa to 0.53 GPa via the incorporation of TA molecule.

Fig. 13 presents the effect of TA on the nanoindentation results of C_3A pastes with high sulfate content. It was found that the addition of TA increases the high stiffness areas ($E > 60$ GPa) assigned to unhydrated C_3A due to the retardation effect. Compared with G1C_3A-DI, G1C_3A-TA has more Hc in volume, accompanied by a reduction in monosulfate and AFt. Specifically, the volume fraction of monosulfate and AFt decreased from 0.24 to 0.20 and 0.71 to 0.65, whereas the volume fraction of Hc increases from 0.04 to 0.14. Furthermore, the average elastic modulus for the hydrates, falling within the range of $E \leq 60$ GPa, exhibited an increase from 15.33 GPa to 20.00 GPa.

As shown in Fig. 13g and h, the deconvolution results of hardness show the different trend as that of elastic modulus. Specifically, the volume fraction of monosulfate increased from 0.33 to 0.56, whereas the volume fraction of AFt decreased from 0.62 to 0.29. However, the average hardness of G1C_3A paste was improved from 0.50 GPa to 0.61 GPa in the presence of TA. These results are summarized in Tables 5 and 6 for detailed comparison. Further research will be conducted to understand this discrepancy.

Indeed, the significant increase in elastic modulus can be attributed to the higher packing density of the hydrates induced by TA. The denser microstructure resulting from the presence of TA likely leads to improved interparticle interactions and enhanced mechanical properties, ultimately contributing to the observed increase in elastic modulus. The comprehensive nanoindentation results

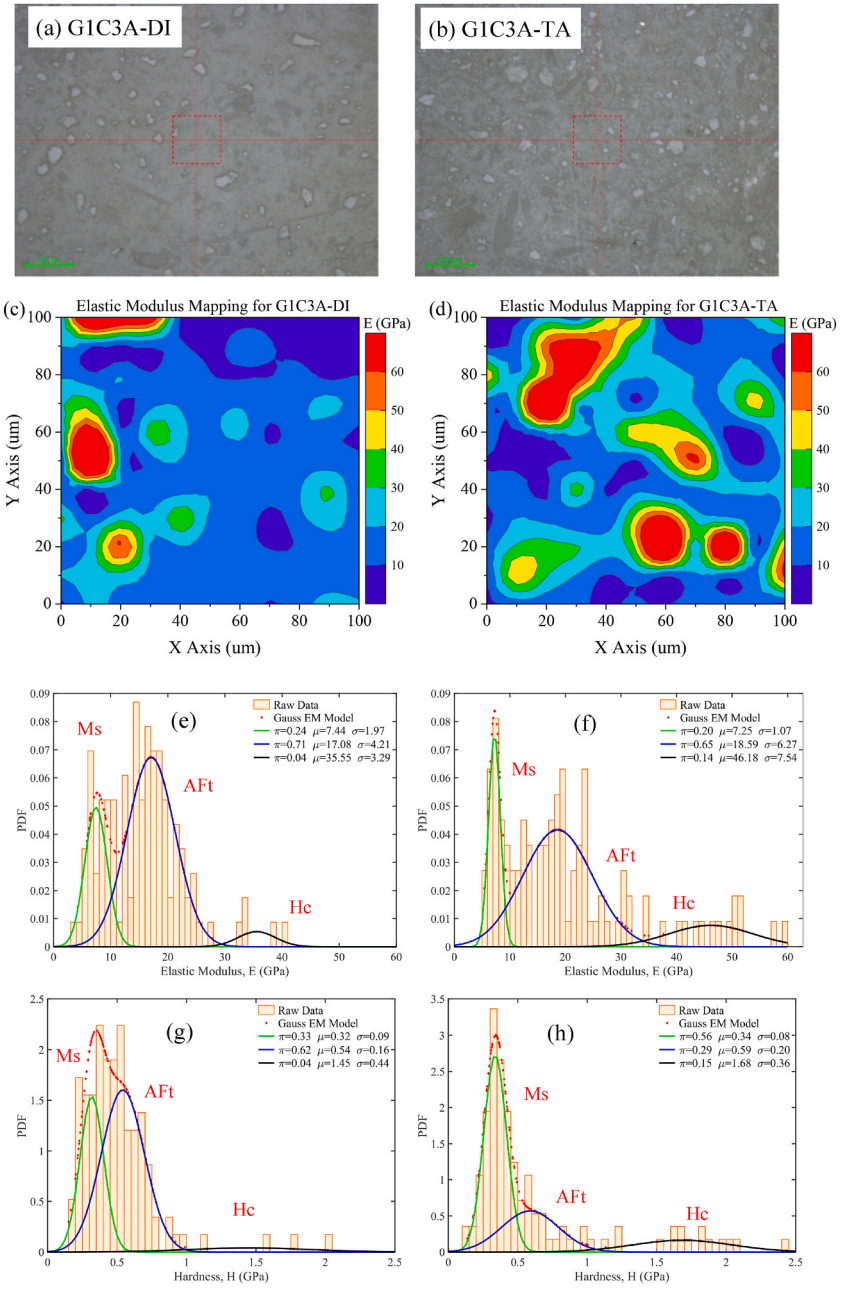

Fig. 13. The nanoindentation results of G1C$_3$A-DI and G1C$_3$A-TA pastes: (a)&(b) microscope images; (c)&(d) the contour mapping of elastic modulus; (e)&(f) the deconvolution results of *Es*; (e)&(f) the deconvolution results of hardness.

Table 5
Elastic modulus (GPa) of different phases of hydrated C$_3$A-gypsum system.

Sample	Ms		AFt		Hc		Average
	Vol.	Mean	Vol.	Mean	Vol.	Mean	
G05C3A-DI	0.59	10.79 ± 2.38	0.38	18.76 ± 2.58	0.03	45.32 ± 9.38	14.85
G05C3A-TA	0.49	10.41 ± 3.08	0.43	19.08 ± 5.49	0.07	34.14 ± 11.68	15.70
G1C3A-DI	0.24	7.44 ± 1.97	0.71	17.08 ± 4.21	0.04	35.55 ± 3.29	15.33
G1C3A-TA	0.20	7.25 ± 1.07	0.65	18.59 ± 6.27	0.14	46.18 ± 7.54	20.00

Table 6
Hardness (GPa) of different phases of hydrated C_3A-gypsum system.

Sample	Ms		AFt		Hc		Average
	Vol.	Mean	Vol.	Mean	Vol.	Mean	
G05C3A-DI	0.68	0.36 ± 0.10	0.32	0.67 ± 0.20	–	–	0.46
G05C3A-TA	0.72	0.40 ± 0.11	0.24	0.71 ± 0.12	0.04	1.74 ± 0.28	0.53
G1C3A-DI	0.33	0.32 ± 0.09	0.62	0.54 ± 0.16	0.04	1.45 ± 0.44	0.50
G1C3A-TA	0.56	0.34 ± 0.08	0.29	0.59 ± 0.20	0.15	1.68 ± 0.36	0.61

across the three scenarios— C_3A, $G05C_3A$, and $G1C_3A$—suggest that TA consistently enhances the micromechanical properties of C_3A-gypsum hydrates, irrespective of the gypsum content. This finding holds significant implications for elucidating the mechanism through which TA enhances the mechanical properties of concrete.

4. Conclusion

This study thoroughly investigates the impact of TA, a naturally occurring plant-based biomolecule, on the hydration of C_3A-gypsum systems. Through detailed analyses of hydration kinetics, hydration product characterization, and micromechanical properties of hydrated C_3A-gypsum pastes, several key conclusions have been drawn.

(1) In the absence of gypsum, the addition of TA accelerates the hydration of C_3A, resulting in a 30.6 % increase in accumulated heat until 10 h. This acceleration is attributed to TA's intercalation with metastable hydration products, such as C_4AH_{13} or C_2AH_8, impeding their transformation into final hydrates (C_3AH_6). XRD, TGA, and FTIR analyses confirm the presence of hexagonal hydrates as the main hydration products in C_3A-TA pastes. Consequently, the average elastic modulus of C3A hydrates significantly increases from 3.83 GPa to 14.28 GPa with the addition of TA, along with an increase in hardness.

(2) In scenarios involving gypsum, the addition of TA markedly retards the hydration of C_3A-gypsum mixtures. This retardation effect is more pronounced in $G1C_3A$, characterized by a high sulfate content (SO_4^{2-}/C_3A molar ratio of 1.57). TA delays the main peaks in heat flow, with significant shifts observed from 4 h to 50 h in $G05C_3A$ and from 16 h to 7 days or longer in $G1C_3A$. Additionally, TA influences the bounding water content of hydration products, increasing it in $G05C_3A$ at 3 days and reducing it in $G1C_3A$ at 7 days. SEM analysis indicates that TA promotes the formation of AFt in $G05C_3A$ while inhibiting its transformation to AFm. Consequently, the average elastic modulus of the paste is enhanced by TA from 14.85 GPa to 15.70 GPa in $G05C_3A$ and from 15.33 GPa to 20.00 GPa in $G1C_3A$, along with an increase in hardness. Furthermore, comprehensive nanoindentation results across all scenarios demonstrate that TA consistently enhances the micromechanical properties of C_3A-gypsum hydrates, regardless of gypsum content. This finding underscores the significant role of TA in improving the mechanical properties of concrete.

In summary, the study provides valuable insights into the mechanisms through which TA influences the hydration kinetics and mechanical properties of C_3A-gypsum systems, offering promising avenues for enhancing the performance of concrete materials.

CRediT authorship contribution statement

Yi Fang: Writing – original draft, Visualization, Methodology, Investigation, Conceptualization. **Jialai Wang:** Writing – review & editing, Resources, Funding acquisition. **Peiyuan Chen:** Investigation. **Zhiang Chen:** Investigation. **Liang Wang:** Investigation. **Xin Qian:** Investigation. **Shifu Liu:** Writing – review & editing, Supervision, Investigation. **Jinxiang Hong:** Investigation.

Declaration of competing interest

The authors declare that they have no known competing financial interests or personal relationships that could have appeared to influence the work reported in this paper.

Data availability

Data will be made available on request.

Acknowledgements

This study was partially supported by the National Science Foundation – United States (CMMI #1761672, ITE #2236331, ITE #2331381), Key Laboratory of Infrastructure Durability and Operation Safety in Airfield of CAAC (MK202301), and National Natural Science Foundation of China (52108187). Any opinions, findings, and conclusions, or recommendations expressed in this material are those of the author(s) and do not necessarily reflect those of the National Science Foundation.

References

[1] T. Hirsch, T. Matschei, D. Stephan, The hydration of tricalcium aluminate (Ca3Al2O6) in Portland cement-related systems: a review, Cement Concr. Res. 168 (2023) 107150.

[2] Y. Cai, D. Xuan, P. Hou, J. Shi, C.S. Poon, Effect of seawater as mixing water on the hydration behaviour of tricalcium aluminate, Cement Concr. Res. 149 (2021) 106565.
[3] A. Ahmed, P. Abubakr, A. Salih Mohammed, Efficient models to evaluate the effect of C3S, C2S, C3A, and C4AF contents on the long-term compressive strength of cement paste, Structures 47 (2023) 1459–1475.
[4] G. Le Saoût, B. Lothenbach, A. Hori, T. Higuchi, F. Winnefeld, Hydration of Portland cement with additions of calcium sulfoaluminates, Cement Concr. Res. 43 (2013) 81–94.
[5] E. Irassar, Sulfate attack on cementitious materials containing limestone filler—a review, Cement Concr. Res. 39 (2009) 241–254.
[6] A. Quennoz, K.L. Scrivener, Hydration of C3A–gypsum systems, Cement Concr. Res. 42 (2012) 1032–1041.
[7] H.F.W. Taylor, Cement Chemistry, Thomas Telford, London, 1997.
[8] X. Ming, W. Si, Q. Yu, Z. Sun, G. Qiu, M. Cao, Y. Li, Z. Li, Molecular insight into the initial hydration of tricalcium aluminate, Nat. Commun. 15 (2024) 2929.
[9] S. Joseph, J. Skibsted, Ö. Cizer, A quantitative study of the C3A hydration, Cement Concr. Res. 115 (2019) 145–159.
[10] S. Pourchet, L. Regnaud, J.-P. Perez, A. Nonat, Early C3A hydration in the presence of different kinds of calcium sulfate, Cement Concr. Res. 39 (2009) 989–996.
[11] R.J. Myers, G. Geng, E.D. Rodriguez, P. da Rosa, A.P. Kirchheim, P.J. Monteiro, Solution chemistry of cubic and orthorhombic tricalcium aluminate hydration, Cement Concr. Res. 100 (2017) 176–185.
[12] R.J. Myers, G. Geng, J. Li, E.D. Rodríguez, J. Ha, P. Kidkhunthod, G. Sposito, L.N. Lammers, A.P. Kirchheim, P.J. Monteiro, Role of adsorption phenomena in cubic tricalcium aluminate dissolution, Langmuir 33 (2017) 45–55.
[13] S. Ye, P. Feng, Y. Liu, J. Liu, J.W. Bullard, Dissolution and early hydration of tricalcium aluminate in aqueous sulfate solutions, Cement Concr. Res. 137 (2020) 106191.
[14] X. Liu, P. Feng, C. Lyu, S. Ye, The role of sulfate ions in tricalcium aluminate hydration: new insights, Cement Concr. Res. 130 (2020) 105973.
[15] Y. Fang, J. Wang, H. Ma, L. Wang, X. Qian, P. Qiao, Performance enhancement of silica fume blended mortars using bio-functionalized nano-silica, Construct. Build. Mater. 312 (2021) 125467.
[16] Y. Fang, J. Wang, X. Qian, L. Wang, P. Chen, P. Qiao, A renewable admixture to enhance the performance of cement mortars through a pre-hydration method, J. Clean. Prod. 332 (2022) 130095.
[17] Y. Fang, J. Wang, X. Qian, L. Wang, Y. Dong, P. Qiao, Low-cost, ubiquitous biomolecule as a strength enhancer for cement mortars, Construct. Build. Mater. 311 (2021) 125305.
[18] Y. Fang, J. Wang, L. Wang, X. Qian, X. Wang, W. Liao, P. Chen, H. Ma, Densifying hydration products of alite by a bio-inspired admixture, Mater. Des. 225 (2023) 111490.
[19] F. Lin, Z. Wang, J. Chen, B. Lu, L. Tang, X. Chen, C. Lin, B. Huang, H. Zeng, Y. Chen, A bioinspired hydrogen bond crosslink strategy toward toughening ultrastrong and multifunctional nanocomposite hydrogels, J. Mater. Chem. B 8 (2020) 4002–4015.
[20] A.E. Hagerman, K.M. Riedl, G.A. Jones, K.N. Sovik, N.T. Ritchard, P.W. Hartzfeld, T.L. Riechel, High molecular weight plant polyphenolics (tannins) as biological antioxidants, J. Agric. Food Chem. 46 (1998) 1887–1892.
[21] A. Arbenz, L. Avérous, Chemical modification of tannins to elaborate aromatic biobased macromolecular architectures, Green Chem. 17 (2015) 2626–2646.
[22] I. Erel-Unal, S.A. Sukhishvili, Hydrogen-bonded multilayers of a neutral polymer and a polyphenol, Macromolecules 41 (2008) 3962–3970.
[23] B. Horev, M.I. Klein, G. Hwang, Y. Li, D. Kim, H. Koo, D.S. Benoit, pH-activated nanoparticles for controlled topical delivery of farnesol to disrupt oral biofilm virulence, ACS Nano 9 (2015) 2390–2404.
[24] P. Kord Forooshani, B.P. Lee, Recent approaches in designing bioadhesive materials inspired by mussel adhesive protein, J. Polym. Sci., Part A: Polym. Chem. 55 (2017) 9–33.
[25] Y. Guan, L. Shao, D. Dong, F. Wang, Y. Zhang, Y. Wang, Bio-inspired natural polyphenol cross-linking poly (vinyl alcohol) films with strong integrated strength and toughness, RSC Adv. 6 (2016) 69966–69972.
[26] J. Plank, D. Zhimin, H. Keller, F.v. Hössle, W. Seidl, Fundamental mechanisms for polycarboxylate intercalation into C3A hydrate phases and the role of sulfate present in cement, Cement Concr. Res. 40 (2010) 45–57.
[27] M. Liu, Y. Gao, L. Zhang, G. Jiang, C. Zeng, P. Wang, The application of thermal analysis to study the hydration behavior of tricalcium aluminate-gypsum in the presence of polycarboxylate-based superplasticizers, Thermochim. Acta 696 (2021) 178821.
[28] S.J. Lee, E.A. Benson, W.M. Kriven, Preparation of Portland cement components by poly (vinyl alcohol) solution polymerization, J. Am. Ceram. Soc. 82 (1999) 2049–2055.
[29] J. Pommersheim, J. Chang, Kinetics of hydration of tricalcium aluminate in the presence of gypsum, Cement Concr. Res. 18 (1988) 911–922.
[30] E. Gartner, J. Young, D. Damidot, I. Jawed, Hydration of Portland Cement, Structure and Performance of Cements, vol. 2, 2002, pp. 57–113.
[31] F. Georget, B. Lothenbach, W. Wilson, F. Zunino, K.L. Scrivener, Stability of hemicarbonate under cement paste-like conditions, Cement Concr. Res. 153 (2022) 106692.
[32] H.-J. Kuzel, H. Pöllmann, Hydration of C3A in the presence of Ca (OH) 2, CaSO4· 2H2O and CaCO3, Cement Concr. Res. 21 (1991) 885–895.
[33] K. Scrivener, R. Snellings, B. Lothenbach, A Practical Guide to Microstructural Analysis of Cementitious Materials, CRC Press Taylor & Francis Group, Boca Raton, 2016.
[34] S.M. Leisinger, B. Lothenbach, G. Le Saout, C.A. Johnson, Thermodynamic modeling of solid solutions between monosulfate and monochromate 3CaO • Al2O3 • Ca[(CrO4)x(SO4)1-x] • nH2O, Cement Concr. Res. 42 (2012) 158–165.
[35] A. Hidalgo Lopez, J.L. García Calvo, J. García Olmo, S. Petit, M.C. Alonso, Microstructural evolution of calcium aluminate cements hydration with silica fume and fly ash additions by scanning electron microscopy, and mid and near-infrared spectroscopy, J. Am. Ceram. Soc. 91 (2008) 1258–1265.
[36] L. Fernández-Carrasco, D. Torrens-Martín, L. Morales, S. Martínez-Ramírez, Infrared spectroscopy in the analysis of building and construction materials, Infrared spectroscopy–Materials science, Eng. Technol. (2012) 369–382.
[37] M. Horgnies, J. Chen, C. Bouillon, Overview about the use of Fourier transform infrared spectroscopy to study cementitious materials, WIT Trans. Eng. Sci. 77 (2013) 251–262.
[38] Q. Liu, X. Ming, M. Wang, Q. Wang, Y. Li, Z. Li, D. Hou, G. Geng, Probing the hydration behavior of tricalcium aluminate under the in situ polymerization of acrylic acid, Cement Concr. Res. 177 (2024) 107429.
[39] A. Rhardane, F. Grondin, S.Y. Alam, Development of a micro-mechanical model for the determination of damage properties of cement pastes, Construct. Build. Mater. 261 (2020) 120514.
[40] S. Hajilar, B. Shafei, Mechanical failure mechanisms of hydrated products of tricalcium aluminate: a reactive molecular dynamics study, Mater. Des. 90 (2016) 165–176.
[41] C. Phrompet, C. Sriwong, C. Ruttanapun, Mechanical, dielectric, thermal and antibacterial properties of reduced graphene oxide (rGO)-nanosized C3AH6 cement nanocomposites for smart cement-based materials, Composites, Part B 175 (2019) 107128.
[42] J. Zhao, C. Sun, Q. Wang, X. Shen, L. Lu, Thermodynamic, mechanical, and electronic properties of ettringite and AFm phases from first-principles calculations, Construct. Build. Mater. 350 (2022) 128777.
[43] Y. Cai, Y. Tao, D. Xuan, X. Zhu, C.S. Poon, Effects of seawater on the formation and mechanical properties of Friedel's salt associated with tricalcium aluminate, Cement Concr. Res. 174 (2023) 107340.
[44] D. Yang, R. Guo, Experimental study on modulus and hardness of ettringite, Exp. Tech. 38 (2014) 6–12.
[45] Y. Cai, Y. Tao, D. Xuan, Y. Sun, C.S. Poon, Effect of seawater on the morphology, structure, and properties of synthetic ettringite, Cement Concr. Res. 163 (2023) 107034.
[46] S. Hajilar, B. Shafei, Nano-scale investigation of elastic properties of hydrated cement paste constituents using molecular dynamics simulations, Comput. Mater. Sci. 101 (2015) 216–226.